# Saturated hydraulic conductivity determined by on ground mono-offset Ground-Penetrating Radar inside a single ring infiltrometer

Emmanuel Léger, Albane Saintenoy, Yves Coquet

# Saturated hydraulic conductivity determined by on ground mono-offset Ground-Penetrating Radar inside a single ring infiltrometer

Emmanuel Léger,[1] Albane Saintenoy,[1] Yves Coquet,[3]

Corresponding author: E. Léger, Department of earth science, Université Paris Sud, Building 504, Orsay, 91405, France. (emmanuel.leger@u-psud.fr)

[1]Université Paris Sud, UMR 8148 IDES,

Orsay, France.

[2]Université Orléans, ISTO/OSUC.,

Orléans, France.

**Abstract.** In this study we show how to use GPR data acquired along the infiltration of water inside a single ring infiltrometer to inverse the saturated hydraulic conductivity. We used Hydrus-1D to simulate the water infiltration. We generated water content profiles at each time step of infiltration, based on a particular value of the saturated hydraulic conductivity, knowing the other van Genuchten parameters. Water content profiles were converted to dielectric permittivity profiles using the Complex Refractive Index Method relation. We then used the GprMax suite of programs to generate radargrams and to follow the wetting front using arrival time of electromagnetic waves recorded by a Ground-Penetrating Radar (GPR). Theoretically, the 1D time convolution between reflectivity and GPR signal at any infiltration time step is related to the peak of the reflected amplitude recorded in the corresponding trace in the radargram. We used this relationship to invert the saturated hydraulic conductivity for constant and falling head infiltrations. We present our method on synthetic examples and on two experiments carried out on sand soil. We further discuss on the uncertainties on the retrieved saturated hydraulic conductivity computed by our algorithm from the van Genuchten parameters.

## 1. Introduction

Soil hydraulic properties, represented by the soil water retention $\theta(h)$ and hydraulic conductivity $K(h)$ functions, dictate water flow in the vadose zone, as well as partitioning between infiltration and runoff. Their evaluation has important implications for modeling available water resources and for flood forecasting. It is also crucial in evaluating the dynamics of chemical pollutants in soil and in assessing the potential of groundwater pollution.

Soil hydraulic functions can be described by several mathematical expression [*Kosugi et al.*, 2002], among them the van Genuchten function [*van Genuchten*, 1980]. The determination of the parameters defining the van Genuchten soil water retention function [*van Genuchten*, 1980] is usually done using laboratory experiments, such as the water hanging column [*Dane and Hopmans*, 2002].

The hydraulic conductivity function can be estimated either in the laboratory, or in situ using infiltration tests. Among the large number of existing infiltration tests [*Angulo-Jaramillo et al.*, 2000], the single [*Muntz et al.*, 1905] or double ring infiltrometers [*Boivin et al.*, 1987] provide the field saturated hydraulic conductivity by applying a positive water pressure on the soil surface, while the disk infiltrometer [*Perroux and White*, 1988; *Clothier and White*, 1981] allows to reconstruct the hydraulic conductivity curve, by applying different water pressures smaller than or equal to zero. For infiltration tests, the volume of infiltrated water versus time is fitted to infer the soil hydraulic conductivity at or close to saturation. These tests are time-consuming and difficult to apply to landscape-scale forecasting of infiltration. Furthermore, their analysis involve various simplifying

assumptions, partly due to the ignorance of the shape of the infiltration bulb. This lack of knowledge on the form of the infiltration bulb has to be filled to get accurate informations on the soil water retention $\theta(h)$ function and consequently on hydraulic conductivity $K(h)$ function. This can be done by water content sensing.

Vereecken [*Vereecken et al.*, 2008] and Evett and Parkin [*Evett and Parkin*, 2005] give a state of the art on the different techniques available for soil moisture measurements. Among the large panel presented, geophysical methods take an important part, mainly because they are contact free and/or easy to use. The most commonly used hydro-geophysical methods are electrical resistivity measurements [*Goyal et al.*, 2006; *Zhou et al.*, 2001] and electromagnetic methods [*Sheets and Hendrickx*, 1995; *Akbar et al.*, 2005]. This paper focuses on the use of Ground-Penetrating Radar (GPR) as a tool for monitoring water infiltration in soil.

For few decades GPR has been known as an accurate method to highlight water variation in soils [*Huisman et al.*, 2003; *Annan*, 2005]. Different techniques are available in the literature for monitoring water content in soils using GPR. Tomography imaging between boreholes during an infiltration has been done by Binley [*Binley et al.*, 2001] and Kowalsky [*Kowalsky et al.*, 2005] among others. Many advances were done during the last years on Off-Ground GPR using full waveform inversion, for instance to invert soil hydraulic properties (Lambot [*Lambot et al.*, 2006, 2009] and Jadoon [*Jadoon et al.*, 2012]). Grote [*Grote et al.*, 2002] and Lunt [*Lunt et al.*, 2005] used two-way travel time variations from a reflector at a known depth to monitor water content variation with time. Finally, multi-offset GPR survey techniques, i.e. CMP[1] or WARR[2], were carried out during infil-

tration processes in the works of Greaves [*Greaves et al.*, 1996] or Mangel [*Mangel et al.*, 2012].

The work presented here is based on mono-offset monitoring of infiltration with on-ground surface GPR as related by Haarder [*Haarder et al.*, 2011], Moysey [*Moysey*, 2010], Lai [*Lai et al.*, 2012], Dagenbach [*Dagenbach et al.*, 2013] and Saintenoy [*Saintenoy et al.*, 2008]. Haarder [*Haarder et al.*, 2011] used a constant offset on-ground GPR coupled with dye tracing to exhibit preferential flows. They found that a GPR was able to map deep infiltration comparing to dye tracer, but they did not manage to resolve the infiltration patterns (by-pass flow, fingering...). Moysey [*Moysey*, 2010] studied the infiltration inside a sand box from the surface with on-ground GPR. He used the reflection from the wetting front as well as from the ground wave and the bottom of the box, to monitor the water content. He also modelled his experiment and estimated the van Genuchten parameters using semblance analysis. As Léger [*Léger et al.*, 2013], he found that the most poorly constrained parameter was $n$. Lai [*Lai et al.*, 2012] used a joint time frequency analysis coupled with grayscale imaging to measure infiltration and drainage in controlled conditions in laboratory. They were able to follow the peak frequency of the GPR wavelet associated with the wetting front using time frequency analysis and then determined the rate of water infiltration in unsaturated zone. Saintenoy [*Saintenoy et al.*, 2008] monitored the wetting bulb during an infiltration from a Porchet infiltrometer. They were able to identify the dimension of the bulb with time and good agreement was found with modelling.

On the continuity of those studies, we present a method for monitoring the wetting front during infiltration using on-ground GPR with fixed offset inside a ring infiltrometer.

The objectives of this paper were i) to check if the proposed method is accurate enough to monitor wetting front during infiltration with different boundary conditions, ii) to invert saturated hydraulic conductivity using the model of Mualem-van Genuchten [*Mualem*, 1976; *van Genuchten*, 1980] , and iii) to analyze the uncertainties using a simplified MC uncertainty analysis. The method has been tested on synthetic examples and on two field data sets.

## 2. Background

### 2.1. Unsaturated Flow Equation

In this study we consider one-dimensionnal vertical water flow in a soil, described by the one-dimensional Richard's equation [*Richards*, 1931]. Its expression in term of water content is

$$\frac{\partial \theta}{\partial t} = \frac{\partial K(\theta)}{\partial z} + \frac{\partial}{\partial z}\left[D(\theta)\frac{\partial \theta}{\partial z}\right], \tag{1}$$

where $K(\theta)$ is the hydraulic conductivity as a function of water content, and $D(\theta)$ is water diffusivity (Childs and Georges-Collis [*Childs and Collis-George*, 1950]), expressed in terms of water content as $D(\theta) = K(\theta)\frac{\partial h}{\partial \theta}$.

### 2.2. Hydraulic Properties Functions

Several mathematical functions exist to model the hydraulic properties of porous media [*Kosugi et al.*, 2002]. We chose the van Genuchten model [*van Genuchten*, 1980] with the relation of Mualem [*Mualem*, 1976], giving the following expression for the water retention curve:

$$\theta(h) = \theta_r + (\theta_s - \theta_r)(1 + (\alpha h)^n)^{\frac{1}{n}-1}, \tag{2}$$

where $\theta_s$ is the saturated water content, $\theta_r$, the residual water content, and $\alpha$ and $n$, two fitting parameters which are respectively linked to the matric potential and the slope of the water retention curve at the inflexion point. The hydraulic conductivity function is described by

$$K(\theta) = K_s \Theta^{\lambda} \left[1 - \left[1 - \Theta^{\frac{n}{n-1}}\right]^{\frac{n}{n-1}}\right]^2, \quad (3)$$

with $K_s$ the saturated hydraulic conductivity, $\Theta = \frac{\theta - \theta_r}{\theta_s - \theta_r}$ the effective saturation and $\lambda$ a factor that accounts for pore tortuosity. The $\lambda$ parameter has an influence on the shape of the hydraulic conductivity function. However in this study we concentrated on the inversion of only one parameter, the saturated hydraulic conductivity. We fixed $\lambda$ equal to 0.5 as reported in [*Mualem*, 1976].

### 2.3. Petrophysical Relationships

Several empirical and conceptual relationships exist to convert soil dielectric permittivity to volumetric water content. Using the fact that the experiments presented here have been made in a quarry of Fontainebleau sand, considered as pure silica, we used the CRIM relation [*Birchak et al.*, 1974; *Roth et al.*, 1990], which relates the relative dielectric permittivity of bulk media, $\varepsilon_b$, to the volumetric summation of each components of it. Thus for a tri-phasic medium comprising water, air and silicium, we obtain

$$\sqrt{\varepsilon_b} = \theta\sqrt{\varepsilon_w} + (1 - \phi)\sqrt{\varepsilon_s} + (\phi - \theta), \quad (4)$$

where $\varepsilon_w = 80.1$, $\varepsilon_s = 2.5$ are respectively the relative dielectric permittivity of water and silica, $\phi$ the porosity and $\theta$ the volumetric water content.

### 2.4. Dielectric Permittivity Versus Electromagnetic Wave Velocity

Surface GPR consists in a transmitting antenna, being a dipole, positioned on the surface, that emits short pulses of spherical electromagnetic (EM) wave in response to an excitation current source, and a receiving antenna, also located at the surface, which converts the incoming EM fields to an electrical signal source to be treated. Following the works of Annan [*Annan*, 1999], the velocity of electromagnetic waves is

$$v = \frac{c}{\sqrt{\varepsilon' \mu_r \frac{1+\sqrt{1+tan^2\delta}}{2}}}, \tag{5}$$

where $\delta$ is the loss factor as a function of the dielectric permittivity, frequency and electrical conductivity, $\varepsilon'$ is the real part of the relative dielectric permittivity, $\mu_r$ the relative magnetic permeability and $c$ is the velocity of EM waves in air equal to 0.3 $m/ns$. Considering the case of non magnetic soil with low conductivity, in the range of 10 MHz to 1 GHz, the real part dominates the imaginary part of the dielectric permittivity and neglecting Debye [*Debye*, 1929] effect, equation (5) reduces to:

$$v = \frac{c}{\sqrt{\varepsilon'}}. \tag{6}$$

We used this equation to compute the travelling time of an EM wave through a layer of soil of known thickness with a given dielectric permittivity.

### 2.5. Electromagnetic Modelling

Numerous techniques are available for simulating GPR data, e.g. ray-based methods (e.g. Cai and McMechan [*Cai and McMechan*, 1995] or Sethian and Popovici [*Sethian and Popovici*, 1999]), time-domain finite-difference full-waveform methods (e.g. Kunz and Luebbers [*Kunz and Luebbers*, 1996] or Kowalsky [*Kowalsky et al.*, 2001]), or finite differences time domain (FDTD) (e.g. Irving and Knight [*Irving and Knight*, 2006]). We

used the GprMax 2D codes of Giannopoulos [*Giannopoulos*, 2005], which uses FDTD modelling to solve the maxwell equations in 2 dimensions.

## 3. Materials and Methods

### 3.1. Experimental Set-up

We studied infiltration of a 5-cm thick water layer inside of a single ring infiltrometer in a sandy soil. The scheme of the apparatus is presented in Figure 1. The single ring infiltrometer was a 1-mm thick aluminum cylinder with a 60-cm diameter, approximately 20-cm high, buried in the soil to a depth of 10 cm. GPR antennae (namely the transmitter T and the receiver R) were set up at a variable distance from the edge of the cylinder, noted $X$, in Figure 1. In all our field experiments, we used a Mala RAMAC system with antennae centered on 1600 MHz, shielded at the top. The inner part of the cylinder was covered with a plastic waterproof sheet. This allowed us to fill the cylinder with water and create an initial 5-cm thick water layer, while preventing infiltration into the sand before starting data acquisition. The beginning of the acquisition was launched by pulling away the plastic sheet to trigger water infiltration. The GPR system was set to acquire a trace every 10 s. With this apparatus, we performed two types of infiltration: i) a falling head infiltration consisting of pulling away the plastic sheet and leaving water to infiltrate into the sand freely with no additional refill, and ii) a constant head infiltration, when water was continuously added to the ring to maintain a 5-cm thick water layer during the infiltration experiment. In the following examples, we will show that GPR data acquired every 10 s during the infiltration experiment can be used to estimate the saturated soil hydraulic conductivity, $K_s$. In all GPR data presented below, we subtracted the average trace and applied an Automatic Gain Control (AGC) to the data in order

to make them clearer. The van Genuchten parameters, $\alpha$, $n$, $\theta_r$, $\theta_i$ of the sand have been determined in laboratory by several classical hanging water column experiments. We assumed arbitrarily a 5 % uncertainty for all the measured parameters. The sand was considered homogeneous. Its initial water content, $\theta_i$, and porosity, $\phi$, of the soil were determined using gravimetric measurements on field samples.

### 3.2. Modelling

Infiltration experiments were simulated by solving Richards equation (Eq. (1) ) using Hydrus-1D. The soil profile was 50 cm deep, assumed to be homogeneous, and divided into 1001 layers. We used either an atmospheric boundary condition (BC) with no rain and no evaporation at the soil surface, for the falling head infiltration, or a constant pressure head of 5 cm to the top node, for the constant head infiltration, and for both case free drainage BC at the bottom. To simulate the 5-cm layer of water, the initial condition was set to a 5 cm pressure head in the top node. We simulated the first 10 minutes of the experiment with a time step of 10 s, i.e., with 60 water content snapshots. Using the CRIM relation (Eq. 4), each water content snapshot was converted to permittivity profiles (made of 1001 points), considering a three-phase media: sand (considered as pure silica), water, and air. Each one of these permittivity profiles were the input for the GprMax2D program [*Giannopoulos*, 2005]. GprMax2D gave simulated GPR monitoring of the infiltration process. We then picked the maximum amplitude of the signal to get the Two Way Travel (TWT) time of the wetting front reflection.

### 3.3. Inversion Algorithm

#### 3.3.1. Convolution Algorithm

Our inversion algorithm was based on the comparison between the arrival times of the wetting front reflection observed in the radargrams acquired during the water infiltration experiment and the arrival times of these reflections computed from the theoretical water content profiles modeled by Hydrus-1D. If a suitable relationship between water content and dielectric permittivity is known, water content profiles, obtained by the resolution of the Richards [*Richards*, 1931] equation (done by Hydrus1D in our case), can be transformed to a 2D series of reflection coefficients:

$$R_{i,t} = \frac{\sqrt{\varepsilon_{i+1,t}} - \sqrt{\varepsilon_{i,t}}}{\sqrt{\varepsilon_{i+1,t}} + \sqrt{\varepsilon_{i,t}}}, \tag{7}$$

where $\sqrt{\varepsilon_{i,t}}$ and $\sqrt{\varepsilon_{i+1,t}}$ are the relative dielectric permittivity at the infiltration time $t$ for two successive model cells centered at depth $z_i$ and $z_{i+1}$.The effective depth where the reflection coefficient is calculated is $z_R = \frac{z_i + z_{i+1}}{2}$. Knowing the dielectric permittivity of each layer of the profile, the electromagnetic wave velocity (Eq. 6) and travel time can be computed. The travel time is used to interpolate reflection coefficients to a constant sampling interval. We used this depth to time conversion to compute a Ricker signal in this time interval. The center frequency of the Ricker was set to 1000 MHz, central frequency of the GPR signal recorded on the field. We derived it twice with respect to time to simulate the transformation made by the emitter and the receiver in real antennae. We then performed the convolution between this pseudo-GPR signal and the reflectivity to obtain

$$O(t) = R(t) * \frac{\partial^2}{\partial t^2} I(t), \tag{8}$$

where $O(t)$ is the output signal, $R(t)$ is the reflectivity and $I(t)$ is the input source of the antenna.

Some remarks have to be made about the comparison between 1D-temporal convolution and real electromagnetic signal. First of all, our inversion algorithm is based on the assumption that soil can be represented as a stack of homogeneous layers. The assumption of horizontal interfaces forces the reflection coefficient (equation (7)) to be expressed as a normal incidence case. Secondly, we considered that the 2-D plane waves computed by FDTD algorithm (modelling) and 3-D plane waves (experiments) could be treated as a 1-D temporal convolution. Third we neglect relaxation effects occurring when propagating an electromagnetic wave in water saturated sand.

#### 3.3.2. Inversion Procedure

We used the TWT time obtained from the radargram (modelled or experimental) as data to be fitted to derive the saturated hydraulic conductivity, assuming the other 4 van Genuchten parameters and initial water content were known. Using Hydrus-1D, we generated 60 water content snapshots using the saturated hydraulic conductivity in the range from 0.01 to 1 $cm/min$, with a step of 0.001 $cm/min$. For each value of $K_s$, we calculated the TWT time using our convolution algorithm and we computed the Root Mean Square Error (RMSE) between these times and the data as an objective function, to be computed as function of saturated hydraulic conductivity. The $K_s$ value which corresponds to the minimum of the objective function was used as inverted value.

## 4. Falling Head Infiltration Experiment

### 4.1. Numerical Example

#### 4.1.1. Forward modelling

The set of hydrodynamical parameters used for this numerical example is presented in Table 1. The permittivity profiles, resulting from water content conversions from Hydrus-

221 1D to permittivity and which were used as input of GprMax2D program [*Giannopoulos*,
222 2005] are presented in Figure 2-a. The simulated GPR monitoring of the infiltration
223 process is shown in Figure 2-b. The horizontal axis is the number of traces simulated
224 with GprMax2D, two traces being separated by 10 seconds, as permittivity profiles are.
225 The vertical axis is the TWT time of the EM wave coming back to the receiver.

226 On the profile presented in Figure 2-b, we denote one particular reflection, labeled A. Its
227 arrival time is increasing as the wetting front moves deeper. This reflection is interpreted
228 as coming from the wetting front. The reflections labeled $A'$ and $A''$ are primary and
229 secondary multiples of reflection $A$. The reflection labeled $B$ is the wave traveling in air
230 directly between the two antennae. After the $40^{th}$ trace, the 5-cm layer of water has been
231 infiltrated, and drainage is starting. As a consequence, the permittivity of the upper part
232 of the medium decreases and the velocity increases (Eq. 6). The TWT time of reflection
233 $A$ increases more slowly, creating a change of slope in the reflection time curve (Fig. 2-b).
234 In Figure 2-c, we display two curves: the TWT time of the maximum peak of reflection $A$
235 (obtained from Figure 2-b) and the TWT time calculated by the convolution Algorithm.

236 The result of the convolution algorithm is in good agreement with the GprMax2D
237 modelling.

238 **4.1.2. Inverse Modeling**

239 We used the TWT time obtained from the radargram of Figure 2-b as data to be
240 fitted to derive the saturated hydraulic conductivity, assuming the other 4 van Genuchten
241 parameters and initial water content were known (see Table 1). The RMSE was minimized
242 for $K_s = 0.121\ cm/min$, which has to be compared with the value set as input, i.e.,

243 $K_s = 0.120\ cm/min$. This result confirms the ability of our algorithm to invert saturated
244 hydraulic conductivity.

## 4.2. Field experiment

### 245 4.2.1. Experimental Data and its Analysis

246 The experiment took place in a quarry of Fontainebleau sand in Cernay-La-Ville (Yve-
247 lines, France). The middle of the antennae was positioned 11 cm away from the cylinder
248 wall ($X = 11\ cm$ in Fig. 1). The 5-cm water layer was fully infiltrated after about 10
249 minutes, although in certain areas of the soil surface this time has been slightly shorter.
250 The sand parameters measured by the hanging water column are given in Table 1 and
251 initial volumetric water content is $\theta_i = 0.09 \pm 0.01\ cm^3/cm^3$. The recorded GPR data
252 are shown in Fig. 3. In this profile, we denote three particular reflections. The one
253 interpreted as coming from the infiltration front, labeled A, is visible during the first 30
254 minutes of the acquisition, with an arrival time varying from 2 ns down to 9 ns. The other
255 reflections come from the cylinder and are interpreted in [*Léger and Saintenoy*, 2012]. We
256 determined the arrival time of the A reflection peak and inverted the saturated hydraulic
257 conductivity using the same algorithm as for the synthetic case. We obtained the mini-
258 mum of the objective function for $K_s = 0.120\ cm/min$. In parallel, we also carried out
259 disk infiltrometer experiments, using the multi-potential method [*Ankeny et al.*, 1991;
260 *Reynolds and Elrick*, 1991]. We obtained a value of the saturated hydraulic conductivity
261 of $K_{Disk} = 0.108 \pm 0.01\ cm/min$.

### 262 4.2.2. Uncertainty Analysis

263 We attempted to evaluate the uncertainty in the saturated hydraulic conductivity re-
264 trieved from GPR data fitting by using a modified Monte Carlo method. We qualified this

method as "modified Monte Carlo" in the sense that it is nor the Tarantola method [*Tarantola*, 1987] and neither the adaptive method proposed by the Guide to the expression of uncertainty in measurement [*BIPM et al.*, 2011] published by the Joint Committee for Guides in Metrology (JCGM). We consider five major uncertainty sources, four from the van Genuchten parameters, $\alpha$, $n$, $\theta_r$, $\theta_s$ and one from the initial water content $\theta_i$. We do assume that all uncertainties can by described by gaussian distribution probability function centered on the value found by several water hanging column experiments with a standard deviation of 5 % of this value. With this definition we obtained the following set of a priori density function for experimental case: $\mathcal{N}_\alpha(\alpha^\mu = 0.023\ cm^{-1},\ \alpha^\sigma = 0.001\ cm^{-1})$, $\mathcal{N}_n(n^\mu = 6.7,\ n^\sigma = 0.3)$, $\mathcal{N}_{\theta_r}(\theta_r^\mu = 0.062\ cm^3/cm^3,\ \theta_r^\sigma = 0.001 cm^3/cm^3)$, $\mathcal{N}_{\theta_s}(\theta_s^\mu = 0.39\ cm^3/cm^3,\ \theta_s^\sigma = 0.01\ cm^3/cm^3)$, and $\mathcal{N}_{\theta_i}(\theta_i^\mu = 0.09\ cm^3/cm^3,\ \theta_i^\sigma = 0.01\ cm^3/cm^3)$, where the $\mathcal{N}$ stands for the gaussian/normal probability density function and the $\mu$ and $\sigma$ represent the mean and standard deviation. We generate multiple sets of parameters by sampling each gaussian distribution, $\{\alpha^i,\ n^i,\ \theta_r^i,\ \theta_s^i,\ \theta_i^i\}$, where the subscript "$i$" is the iteration number. For each set the value of $K_s$ minimising the objective function was computed by our inversion procedure presented above. We generated enough sets of parameters such as the histogram of $K_s$ values look like a gaussian function with a stabilized standard deviation. We used this standard deviation as uncertainty on $K_s$.

We did not consider the uncertainties on radargram picking, because we evaluated it has a very weak influence comparing to the other uncertainties considered.

Using our analysis, we found in the case of falling head infiltration that $K_s$ was equal to $0.12 \pm 0.01\ cm/min$. This narrow range of possible values is in agreement with disk infiltrometer value, and clearly shows the accuracy of our method.

## 5. Constant Head Infiltration Experiment

### 5.1. Numerical Example

#### 5.1.1. Forward Modelling

In this second case, a water layer of 5 cm above the ground was kept constant during the entire experiment. Similarly as above, using the same van Genuchten parameters as in the first synthetic example (Table 1), we modeled infiltration of water inside a ring infiltrometer by applying a constant pressure head of 5 cm to the top node during 10 minutes. The permittivity profiles are presented in Fig. 4-a, with each curve plotted every 10 s as in the previous case. Fig. 4-b shows the radargram simulated with GprMax2D. As can be seen, the reflection labeled $A$ describing the position of the infiltration front, is returning at increasing times, because infiltration is being constantly fed by the constant ponding depth, contrary to the previous falling head case. In Fig. 4-c, we computed the TWT time of the wetting front using the convolution algorithm and picking the $A$ reflection from the radargram in Fig. 4-b.

#### 5.1.2. Inverse Modelling

We inverted for the saturated hydraulic conductivity by minimizing the differences between the arrival times of the wetting front reflection obtained by the convolution algorithm and the arrival times picked from the simulated radargram in Fig. 4-b. The objective function was minimized for $K_s = 0.119\ cm/min$, to be compared with the value used for simulating the data: $K_s = 0.120\ cm/min$.

### 5.2. Field Experiment

The experiment took place in the same quarry of Fontainebleau sand as the previous experiment. The middle of the antennae was positioned in the middle of the ring (X = 30

cm in Fig. 1). The GPR data are shown in Fig. 5 and were recorded during 80 minutes (only a part of the radargram is presented). We used the van Genuchten parameters determined in the laboratory using the hanging column experiments (Table 1) and we measured on sand core samples an initial volumetric water content of $\theta_i = 0.07 \pm 0.02$.

In the profile presented in Fig. 5, the arrival time of reflection $A$ ranges from 0 at the beginning of the experiment to about 6 ns after 10 min. We picked the arrival time of the $A$ reflection peak and computed the objective function using the same procedure as described before. We obtained the minimum of the objective function for $K_s = 0.089\ cm/min$. Again, this value has to be compared with the one obtained by the disk infiltrometer experiment, $K_{Disk} = 0.108 \pm 0.01\ cm/min$. Using the same procedure as presented in the earlier field example, we found a range of possible values for the saturated hydraulic conductivity, $K_s = 0.089 \pm 0.005\ cm/min$. Despite the fact that we are not in the same range as the disk infiltrometer method the discrepancy is very small and allows us to conclude on the good accuracy of our method.

## 6. Discussion

The results presented above indicate clearly that a commercial surface GPR can be used as a tool for monitoring the wetting front. Although the use of surface-based GPR data to estimate the parameters of unsaturated flow models is not new [*Moysey*, 2010], our method gives accurate values of the saturated hydraulic conductivity with uncertainties comparable or smaller than those obtained with disk infiltrometer measurements. A distinct advantage of our approach is the simplicity of the algorithm and its rapidity to converge, which is very encouraging for more complicated models ( stack of non-homogeneous layers).

The discrepancy between saturated hydraulic conductivity determined by disk infiltrometry and that obtained with our GPR algorithm comes from different phenomena. First of all, the van Genuchten parameters determined from the water hanging column experiment are obtained with saturation coming from the bottom of the soil samples, whereas in our case, the infiltration is a ponded one, thus coming from the top.

Despite the fact that we upgraded the single ring infiltrometer by the use of GPR to monitor the wetting front, we still suffer from the problem of entrapped-air, which causes reduction of saturated water content and hydraulic conductivity. This issue cannot be fixed with ponded infiltration. Disk infiltrometer measurement monitoring may cause less problems, working with negative matric potentials [*Ankeny et al.*, 1991; *Reynolds and Elrick*, 1991].

During our modeling, we considered our soil as an homogeneous and isotropic one. Real soils exhibit heterogeneities, triggering preferential flows. Even in the case of our quarry of Fontainebleau sand, differences in packing and compaction could lead to creation of preferential flow paths.

One of the way to solve this issue could be to use a dual porosity model [*Gerke and van Genuchten*, 1993] and a Monte Carlo procedure to generate a high number of soil models with different parameters, as we did with the single porosity model in Hydrus-1D, and performed statistical analysis on the saturated hydraulic conductivity obtained.

An other source of error, already discussed above, comes from the assumption that a 3D infiltration monitored by 3D electromagnetic waves can be treated as a 1-D temporal convolution. This limitation will be studied in future works, using Hydrus 2D/3D to simulate 2D axisymmetrical infiltration and 2D infiltration.

The results represent a promising step toward application of multi-parameters inversions. A first study in that direction was presented in Léger [*Léger et al.*, 2013].

## 7. Summary

This research investigated the use of on-ground surface GPR to monitor the wetting front during infiltration inside a ring infiltrometer. We showed by modeling and experiments that a standard GPR device was able to monitor the displacement of the water front in the soil. We tested in synthetic cases the ability of our algorithm to invert the saturated hydraulic conductivity, knowing the other van Genuchten parameters and the initial water content. Two infiltration experiments were performed, falling head infiltration and constant head infiltration, in a quarry of Fontainebleau sand. The retrieved saturated hydraulic conductivity was comparable to that obtained with disk infiltrometer experiments. Uncertainty analysis accounting for all the van Genuchten parameters, was performed using a modified Monte Carlo method, and proved the robustness of our algorithm. Although results retrieved with GPR were in agreement with disk infiltrometry tests, we stress that further research is needed to improve our algorithm so as to determine the whole set of soil hydrodynamic parameters.

## Notes

1. Common MidPoints

2. Wide-Angle Reflection- Refraction

## References

Akbar, M., A. Kenimer, S. Searcy, and H. Tobert (2005), Soil water estimation using electromagnetic induction, *Trans. ASAE*, *48*(1), 129–135.

371 Angulo-Jaramillo, R., J.-P. Vandervaere, S. Roulier, J.-L. Thony, J.-P. Gaudet, and
372 M. Vauclin (2000), Field measurement of soil surface hydraulic properties by disc and
373 ring infiltrometers: A review and recent developments, *Soil and Tillage Research*, *55*(1),
374 1–29.

375 Ankeny, M., M. Ahmed, T. Kaspar, and R. Horton (1991), Simple field method for deter-
376 mining unsaturated hydraulic conductivity, *Soil Sci. Sco. Am. J.*, *55*(2), 467–470.

377 Annan, A. (1999), Ground penetrating radar: Workshop notes, *Tech. rep.*, Sensors and
378 Software Inc., Ontario, Canada.

379 Annan, A. P. (2005), Gpr methods for hydrogeological studies, in *Hydrogeophysics*, pp.
380 185–213, Springer.

381 Binley, A., P. Winship, R. Middleton, M. Pokar, and J. West (2001), High-resolution
382 characterization of vadoze zone dynamics using cross-borehole radar, *Water Ressources*
383 *Research*, *37*(11), 2639–2652.

384 BIPM, IEC, IFCC, ILAC, ISO, IUPAC, IUPAP, and OIML. (2011), *Evaluation of mea-*
385 *surement data — Supplement 2 to the - Guide to the expression of uncertainty in mea-*
386 *surement" - Models with any number of output quantities.*, Joint Committee for Guides
387 in Metrology, JCGM:102.

388 Birchak, J., L. Gardner, J. Hipp, and J. Victor (1974), High dielectric constant microwave
389 probes for sensing soil moisture, *Procedings IEEE*, *35*(1), 85–94.

390 Boivin, P., J. Touma, and P. Zante (1987), Mesure de l'infiltrabilité du sol par la méthode
391 du double anneau. 1-Résultats expérimentaux, *Cahiers ORSTOM, Sér. Pédol.*, *24*(1),
392 17–25.

393 Cai, J., and G. A. McMechan (1995), Ray-based synthesis of bistatic ground penetrating
394 radar profiles., *Geophysics*, *60*(1), 87–96.
395 Childs, E., and N. Collis-George (1950), The permeability of porous materials, *Proc. Roy.*
396 *Soc.*, *201*(1066), 392–405.
397 Clothier, B., and I. White (1981), Measuring sorptivity and soil water diffusivity in the
398 field., *Soil Sci. Am. J.*, *45*(2), 241–245.
399 Dagenbach, A., J. Buchner, P. Klenk, and K. Roth (2013), Identifying a parametrisation of
400 the soil water retention curve from on-ground GPR measurements., *Hydrological Earth*
401 *System Science*, *17*(1), 611–618.
402 Dane, J. H., and J. W. Hopmans (2002), *Method of soil analysis, Part 4, Physical method*,
403 pp. 680–684, Soil Science Society od America, Inc., Madison, WI.
404 Debye, P. (1929), *Polar Molecules*, Dover Publications, New York.
405 Evett, S., and G. Parkin (2005), Advances in soil water content sensing: The continuing
406 maturation of technology and theory, *Vadose Zone Journal*, *4*(4), 986–991.
407 Gerke, H., and M. T. van Genuchten (1993), A dual porosity model for simulating the pref-
408 erential movement of water and solutes in structured porous media, *Water Ressources*
409 *Research*, *29*(2), 305–319.
410 Giannopoulos, A. (2005), Modelling ground penetrating radar by GprMax, *Construction*
411 *and Building Materials*, *19*(10), 755–762.
412 Goyal, V., P. Gupta, S. Seth, and V. Singh (2006), Estimation of temporal changes in soil
413 moisture using resistivity method, *Hydrological Processes*, *10*(9), 1147–1154.
414 Greaves, R., D. Lesmes, J. Lee, and M. Toksoz (1996), Velocity variations and water
415 content estimated from multi-offset ground-penetrating radar, *Geophysics*, *61*(3), 683–

695.

Grote, K., S. Hubbard, and Y. Rubin (2002), Gpr monitoring of volumetric water content in soils applied to highway construction and maintenance, *The Leading Edge*, *21*(5), 482–485.

Haarder, E., M. L. K. Jensen, and L. Nielsen (2011), Visualizing unsaturated flow phenomena using high-resolution reflection ground penetrating radar, *Vadose Zone Journal*, *10*(1), 84–97.

Huisman, J., S. Hubbard, J. Redman, and A. Annan (2003), Measuring soil water content with ground-penetrating radar: A review, *Vadoze Zone Journal*, *2*(4), 476–491.

Irving, J., and R. Knight (2006), Numerical modeling of ground-penetrating radar in 2D using Matlab, *Computers and Geosciences*, *32*(9), 1247–1258.

Jadoon, K., L. Weihermüller, B. Scharnagl, M. Kowalsky, M. Bechtold, S. Hubbard, H. Vereecken, and S. Lambot (2012), Estimation of soil hydraulic parameters in the field by integrated hydrogeophysical inversion of time-lapse ground-penetrating radar, *Vadose Zone Journal*, *11*(4).

Kosugi, K., J. Hopmans, and J. Dane (2002), *Methods of Soil Analysis*, chap. Parameretric models, Soil Science Society of America.

Kowalsky, M., P. Dietrich, G. Teutsch, and Y. Rubin (2001), Forward modeling of ground-penetrating radar using digitized outcrop images and multiple scenarios of water saturation, *Water Ressources Research*, *37*(6), 1615–1626.

Kowalsky, M., S. Finsterle, J. Peterson, S. Hubbard, Y. Rubin, E. Majer, A. Ward, and G. Gee (2005), Estimation of field-scale soil hydraulic and dielectric parameters through joint inversion of GPR and hydrological data, *Water Ressources Research*,

*41*(11), W11,425.1–W11,425.19.

Kunz, K., and R. Luebbers (1996), *The finite Difference Time domain Method for Electromagnetics*, CRC Press.

Lai, W., S. Kou, and C. Poon (2012), Unsaturated zone characterization in soil through transient wetting and drying using GPR joint time-frequency analysis and grayscale images, *Journal of Hydrology*, *452-453*, 1–13.

Lambot, S., E. Slob, M. Vanclooster, and H. Vereecken (2006), Closed loop GPR data inversion for soil hydraulic and electric property determination., *Geophysical research letters*, *33*(21), L21,405.1–L21,405.5.

Lambot, S., E. Slob, J. Rhebergen, O. Lopera, K. Jadoon, and H. Vereecken (2009), Remote estimation of the hydraulic properties of a sand using full-waveform integrated hydrogeophysical inversion of time-lapse, off ground GPR data, *Vadose Zone Journal*, *8*(3), 743–754.

Léger, E., and A. Saintenoy (2012), Surface ground-penetrating radar monitoring of water infiltration inside a ring infiltrometerenetrating radar monitoring of water infiltration inside a ring infiltrometer, in *14th International Conference on Ground Penetrating Radar*, Shanghai.

Léger, E., A. Saintenoy, and Y. Coquet (2013), Estimating saturated hydraulic conductivity from surface ground-penetrating radar monitoring of infiltration, in *4th International Conference Hydrus Software Applications to Subsurface Flow and Contaminant Transport Problems*, Pragues.

Lunt, I., S. Hubbard, and Y. Rubin (2005), Soil moisture content estimation using ground-penetrating radar reflection data, *Journal of Hydrology*, *307*(1-4), 254–269.

462 Mangel, A., S. Moysey, J. Ryan, and J. Tarbutton (2012), Multi-offset ground-penetrating
463 radar imaging of a lab-scale infiltration test, *Hydrological Earth System Science Discus-*
464 *sions*, *16*, 4009–4022.

465 Moysey, S. (2010), Hydrologic trajectories in transient ground-penetrating-radar reflection
466 data, *Geophysics*, *75*(4), WA211–WA219.

467 Mualem, Y. (1976), A new model for predicting the hydraulic conductivity of unsaturated
468 porous media., *Water Resour. Res.*, *12*(3), 513–522.

469 Muntz, A., L. Faure, and E. Laine (1905), Etudes sur la perméabilité des terres, faites en
470 vue de l'arrosage, *Ann. De la Direction de l'Hydraulique*, *f33*, pp. 45–53.

471 Perroux, K., and I. White (1988), Designs for disc permeameters, *Soil Sci. Sco. Am. J.*,
472 *52*(5), 1205–1215.

473 Reynolds, W., and D. Elrick (1991), Determination of hydraulic conductivity using a
474 tension infiltrometer, *Soil Sci. Sco. Am. J.*, *55*(3), 633–639.

475 Richards, L. (1931), Capillary conduction of liquids through porous medium, *Physics 1*,
476 pp. 318–333.

477 Roth, K., R. Schulin, H. Fluhler, and W. Attinger (1990), Calibration of time domain
478 reflectometry for water content measurement using a composite dielectric approach,
479 *Water Ressources Research*, *26*(10), 2267–2273.

480 Saintenoy, A., S. Schneider, and P. Tucholka (2008), Evaluating ground-penetrating radar
481 use for water infiltration monitoring, *Vadose Zone Journal*, *7*(1), 208–214.

482 Sethian, J., and A. Popovici (1999), 3-d travel time computation using the fast marching
483 method, *Geophysics*, *64*(2), 516–523.

| Falling Head Infiltration | | | | | | | |
|---|---|---|---|---|---|---|---|
| | $\theta_i$ | $\theta_r$ | $\theta_s$ | $\alpha$ ($cm^{-1}$) | $n$ | $K_s$ (cm/min) | Retrieved $K_s$ (cm/min) |
| Numerical | 0.17 | 0.07 | 0.43 | 0.019 | 8.67 | 0.120 | 0.121 |
| Field | 0.09 $\pm$0.01 | 0.062 $\pm$0.003 | 0.39 $\pm$0.01 | 0.023 $\pm$0.001 | 6.7 $\pm$0.3 | 0.108 $\pm$0.01* | 0.120 $\pm$0.013 |
| Constant Head Infiltration | | | | | | | |
| | $\theta_i$ | $\theta_r$ | $\theta_s$ | $\alpha$ ($cm^{-1}$) | $n$ | $K_s$ (cm/min) | Retrieved $K_s$ (cm/min) |
| Numerical | 0.17 | 0.07 | 0.43 | 0.019 | 8.67 | 0.120 | 0.119 |
| Field | 0.07 $\pm$0.02 | 0.062 $\pm$0.003 | 0.39 $\pm$0.01 | 0.023 $\pm$0.001 | 6.7 $\pm$0.3 | 0.108 $\pm$0.01* | 0.089 $\pm$0.009 |

**Table 1.** Hydrodynamic parameters for the numerical and field experiment. The * indicates values of $K_s$ measured from disk infiltrometer experiments.


Sheets, K., and J. Hendrickx (1995), Non invasive soil-water content measurement using electromagnetic induction, *Water Ressources Research*, *31*(10), 2401–2409.

Tarantola, A. (1987), *Inverse Problem Theory*, Elsevier, New York.

van Genuchten, M. T. (1980), A closed-form equation for predicting the hydraulic conductivity of unsatured soils, *Soil Sci. Soc. Am. J.*, *5*(44), 892–898.

Vereecken, H., J. Huisman, H. Bogena, and J.Vanderborght (2008), On the value of soil moisture measurements in vadose zone hydrology: A review, *Water Ressources Research*, *44*(4), 1–21.

Zhou, Q., J. Shimada, and A. Sato (2001), Three-dimensionnal spatial and temporal monitoring of soil water content using electrical resistivity tomography, *Water Ressources Research*, *37*(2), 273–285.

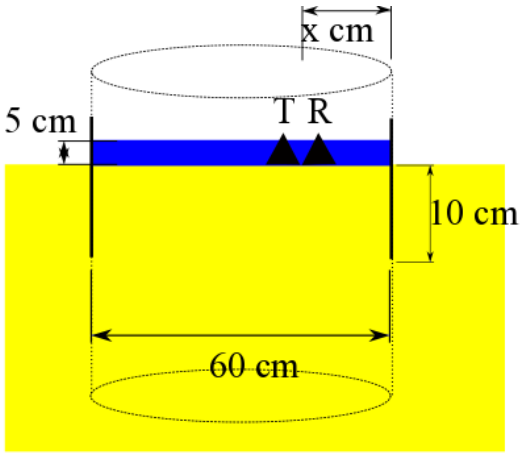


**Figure 1.** Experimental set up at its initial state.

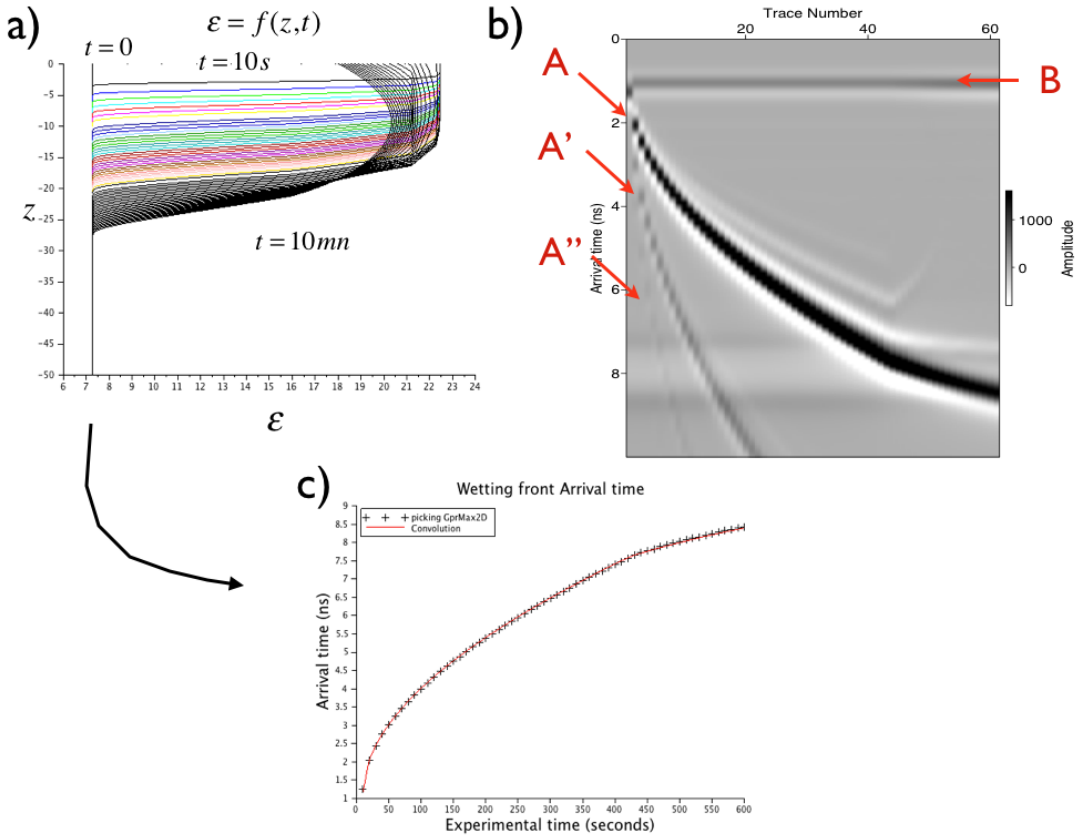


**Figure 2.** Falling head infiltration from a 5-cm thick water layer. a) Permittivity profiles: each curve is plotted every 10 s. b) Radargram simulated with GprMax2D; reflection A is coming from the wetting front, B is the direct wave, A' and A" are multiples of reflection A. c) TWT time computed by the convolution algorithm from the permittivity profiles (plain red line) and TWT time obtained by picking of A peak in fig b).

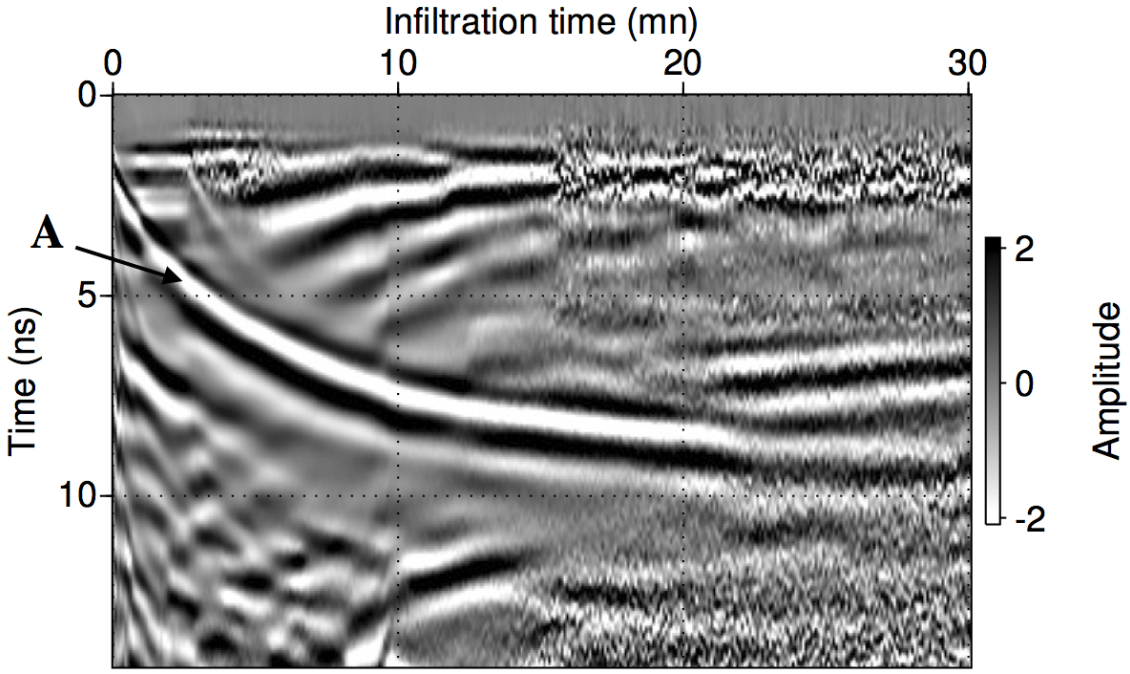


**Figure 3.** Experimental GPR data acquired during the falling head infiltration (using a 5-cm initial water layer). Reflection A is the reflection coming from the wetting front

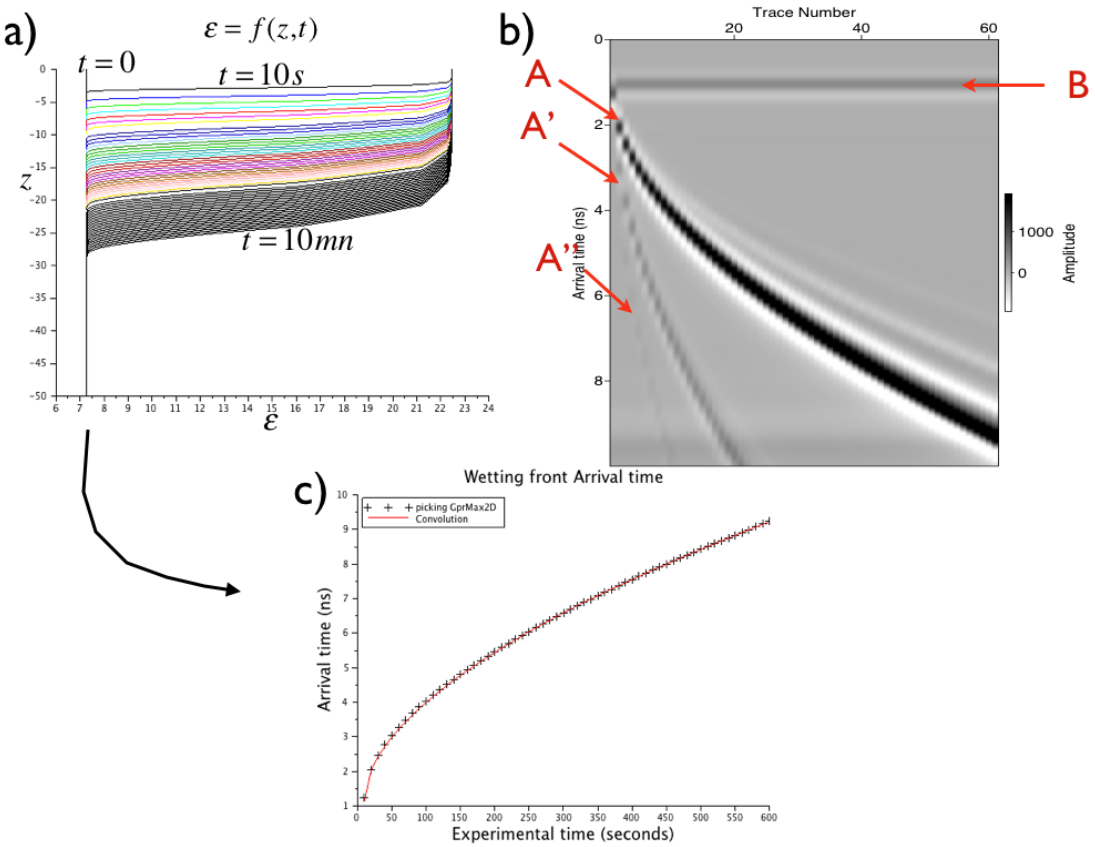


**Figure 4.** Constant head infiltration with 5 cm of water. a) Permittivity profiles, each curve is plotted every 10 s. b) Radargram simulated with GprMax2D, reflection A is the wetting front, B is the direct wave, A' and A" are multiples. c) Two Way Travel Time computed with our convolution algorithm from the simulated permittivity profiles.

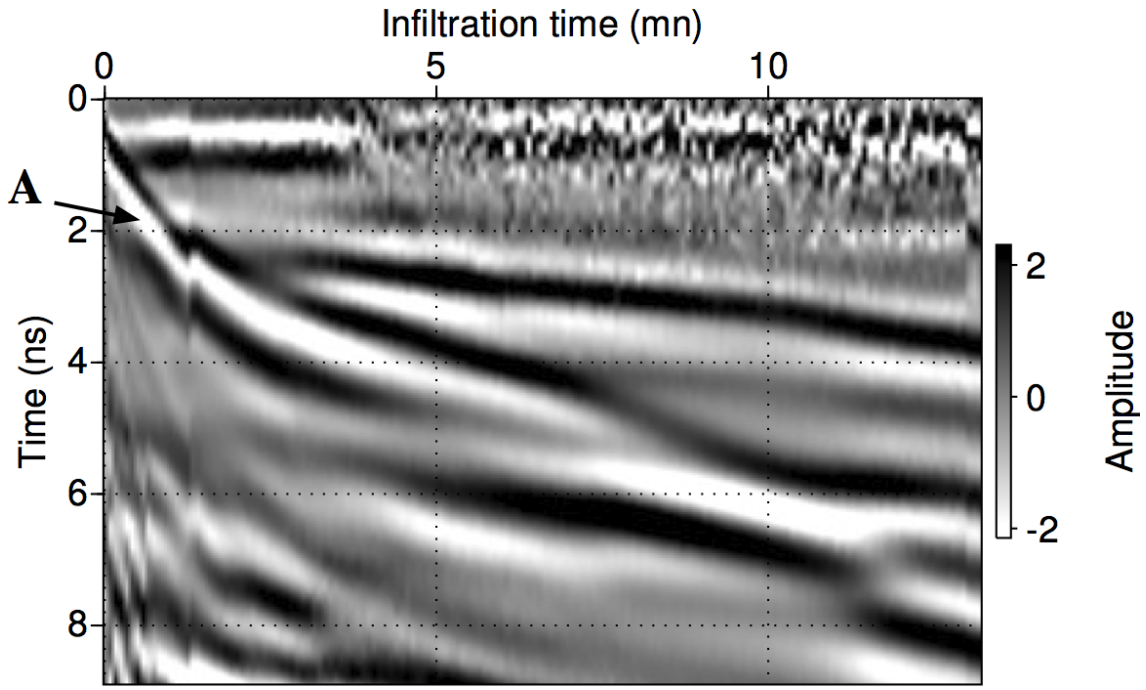


**Figure 5.** GPR data acquired during a constant head (5 cm) infiltration. Reflection A is the reflection coming from the wetting front.